



Ladder-type heteroacene-based dopant-free hole-transporting materials for efficient and stable CsPbI₂Br perovskite solar cells

Hao Liu^{a,b}, Qisheng Tu^a, Di Wang^{a,b}, Qingdong Zheng^{a,*}

^a State Key Laboratory of Structural Chemistry, Fujian Institute of Research on the Structure of Matter, Chinese Academy of Sciences, 155 Yangqiao West Road, Fuzhou, Fujian, 350002, China

^b School of Physical Science and Technology, ShanghaiTech University, 100 Haik Road, Shanghai, 201210, China

ARTICLE INFO

Keywords:

Perovskite solar cells
Hole-transporting materials
Dopant-free
Ladder-type heteroacene
Stability

ABSTRACT

Dopant-free hole-transporting materials (HTMs) play a vital role in improving the power conversion efficiencies (PCEs) and stability for all-inorganic perovskite solar cells (PVSCs). In this work, two donor-acceptor-donor (D-A-D) type HTMs (L2 and L2-T) were designed and synthesized by using a ladder-type heteroacene core. Compared to L2-T with thiophene spacers, L2 presents suitable energy levels, smooth surface morphology, and improved hole mobility. Consequently, CsPbI₂Br PVSC based on L2 delivers a decent PCE of 12.41%, which outperforms the counterpart based on L2-T (11.07%). Whereas, the control device based on dopant-free 2,2',7,7'-tetrakis(*N,N*-di-*p*-methoxyphenylamine)-9,9'-spirobifluorene (Spiro-OMeTAD) reveals a relatively low PCE of 9.95%. In addition, both the L2- and L2-T-based devices can maintain over 85% of their original PCEs after 1000 h storage demonstrating their excellent shelf stability. This work highlights the good potential of the ladder-type heteroacene building block for developing dopant-free HTMs toward high-performance CsPbI₂Br PVSCs.

1. Introduction

Organic-inorganic hybrid perovskite solar cells (PVSCs) have received tremendous attention due to their rapidly increased power conversion efficiencies (PCEs) from 3.8% in 2009 to 25.5% currently [1, 2]. However, the organic-inorganic hybrid perovskites may exhibit poor stability against the light and heat because of the volatilizable organic A-site cations such as methylammonium (MA⁺) and formamidinium (FA⁺) [3,4]. Therefore, replacing the organic cations with inorganic cations to construct all-inorganic perovskites is an emerging strategy in order to improve the stability [5,6]. Hitherto, CsPbI₃ and CsPbI₂Br are two widely used perovskites for all-inorganic PVSCs, and the best PCEs over 16% have been achieved with improved thermal- and photo-stability [7–10].

On the other hand, high-performance HTMs are crucial to achieving efficient and stable PVSCs [11,12]. The HTMs not only play an essential role in promoting hole transport and reducing charge recombination, but also prevent the device from being corroded by moisture, oxygen, and electrode [13]. It is well known that 2,2',7,7'-tetrakis(*N,N*-di-*p*-methoxyphenylamine)-9,9'-spirobifluorene (Spiro-OMeTAD) is the dominated HTM for high-performance PVSCs. However, the orthogonal molecular conformation of Spiro-OMeTAD is not beneficial to form close

molecular π - π stacking, resulting in relatively low hole mobility [14,15]. Thus, the Spiro-OMeTAD always needs to be chemically doped with dopants such as lithium bis(trifluoromethanesulfonyl)imide (LiTFSI), tris(2-(1*H*-pyrazol-1-yl)-4-*tert*-butylpyridine)cobalt(III) tris(bis(trifluoromethylsulfonyl)imide) (FK209), and 4-*tert*-butylpyridine (*t*-BP) to enhance the electrical properties. Nevertheless, most dopants possess ionic diffusion/migration issues and are of the hydrophilic feature, which would aggravate device degradation [16]. Therefore, it is needed to develop alternative dopant-free HTMs for efficient and stable all-inorganic PVSCs.

Donor-acceptor-donor (D-A-D) design strategy has been successfully used in high-performance dopant-free HTMs because the intramolecular charge transfer (ICT) feature of the resulting materials could induce self-doping to facilitate charge extraction [17,18]. Meanwhile, the band gaps, energy levels, and charge transport properties can be easily adjusted by introducing different donor and acceptor units [19]. To date, a number of efficient D-A-D type HTMs for organic-inorganic hybrid PVSCs have been reported [19–22]. For example, Guo et al. designed and synthesized a novel D-A-D type HTM (MPA-BTTI) with well-matched energy levels, moderate hole mobility, and superior film morphology, leading to an outstanding PCE of 21.17% for organic-inorganic hybrid PVSCs [20]. Compared with the enormous

* Corresponding author.

E-mail address: qingdongzheng@fjirm.ac.cn (Q. Zheng).

<https://doi.org/10.1016/j.dyepig.2021.109368>

Received 19 January 2021; Received in revised form 29 March 2021; Accepted 30 March 2021

Available online 6 April 2021

0143-7208/© 2021 Elsevier Ltd. All rights reserved.

efforts devoted in the D-A-D type HTMs for organic-inorganic hybrid PVSCs, much less attention has been paid on the development of dopant-free HTMs for all-inorganic PVSCs in spite of their advantages in stability.

Ladder-type heteroacenes are promising building blocks for efficient D-A-D type HTMs because their energy levels could be easily tuned through the employment of different ladder-type heteroacenes [20, 23–25]. At the same time, the coplanar configuration can effectively strengthen the π - π packing in film state, leading to enhanced charge transport [26,27]. Moreover, the ladder-type heteroacene-based HTMs may exhibit good thermal and chemical stability, which is essential for stable PVSCs [28]. As an electron-deficient ladder-type heteroacene, thieno[2',3':5,6]pyrido[3,4-g]thieno[3,2-c]-isoquinoline-5,11(4H, 10H)-dione (TPTI) has been successfully used in organic solar cells with intriguing photovoltaic performance [29,30]. The nitrogen (N) atoms located at the two electron-withdrawing lactam groups in TPTI can provide sites for introducing alkyl chains which is important to modify the solubility and aggregation. Meanwhile, sulfur (S) atoms and carbonyls in TPTI can act as Lewis base to passivate surface defects of perovskite [31–33]. Therefore, TPTI may be an excellent acceptor core for dopant-free HTMs. However, to the best of our knowledge, TPTI has never been used to construct HTMs for PVSCs. Based on these considerations, two novel D-A-D type dopant-free HTMs (L2 and L2-T) were designed and synthesized by using TPTI as acceptor unit. 4-Methoxy-N-(4-methoxyphenyl)-N-phenylaniline (TPA) was chosen as a donor unit, which is closely related to the hole injection/transportation [34–36]. Both of the newly synthesized HTMs exhibited well-matched energy levels, smooth film morphologies, and high hole mobilities. The dopant-free L2-based device achieved an impressive PCE of 12.41%, with an open-circuit voltage (V_{OC}) of 1.21 V, a short-circuit current density (J_{SC}) of 13.73 mA cm⁻², and a fill factor (FF) of 75.02%, which is superior to the device based on L2-T (11.07%). In contrast, the dopant-free Spiro-OMeTAD-based device showed an inferior PCE of 9.95%. Furthermore, L2- and L2-T-based devices could maintain over 85% of their initial PCEs after 1000 h demonstrating their excellent long-term stability.

2. Experimental section

2.1. Materials

Unless otherwise noted, all chemicals were purchased from Aldrich Inc., Adamas-beta Ltd., Suna Tech Inc., and Energy Chemical without further purification. Lead iodide (PbI₂) and lead bromide (PbBr₂) were purchased from TCI. Cesium iodide (CsI) was purchased from Xi'an Polymer Technology Crop. Spiro-OMeTAD was purchased from Shenzhen Feiming Science and Technology Co., Ltd. The SnO₂ colloid precursor was purchased from Alfa Aesar (Tin (IV) oxide, 15% in H₂O colloidal dispersion).

2.2. Synthesis of HTMs

2.2.1. Synthesis of L2

2,8-Dibromo-4,10-bis(2-hexyldecyl)-4,10-dihydrothieno[2',3':5,6]pyrido[3,4-g]thieno[3,2-c]isoquinoline-5,11-dione (TPTI-Br, 0.100 g, 0.107 mmol), compound **3a** (0.142 g, 0.329 mmol), and Pd(PPh₃)₄ (0.016 g, 0.014 mmol) were dissolved in toluene (25 mL) and K₂CO₃ aqueous solution (2 M, 6 mL). After being degassed with nitrogen for 30 min, the mixture was stirred and reacted at 100 °C for 24 h. Upon cooling down to room temperature, the solution was extracted with CH₂Cl₂ and dried over anhydrous MgSO₄. After concentration, the crude product was purified by column chromatography with petroleum ether/CH₂Cl₂ (1/1, v/v) as eluent to obtain L2 (0.120 g, 81.6% yield) as a yellow solid. ¹H NMR (CDCl₃, 400 MHz, ppm): 8.77 (s, 2H), 7.44 (d, *J* = 8.5 Hz, 4H), 7.10 (m, 10H), 6.94 (d, *J* = 8.5 Hz, 4H), 6.86 (m, 8H), 4.22 (s, 4H), 3.80 (s, 12H), 2.01 (s, 2H) 1.51–1.04 (m, 48H), 0.94–0.67 (m,

12H). ¹³C NMR (CDCl₃, 101 MHz, ppm): 161.65, 156.44, 149.33, 144.70, 140.26, 139.93, 129.60, 127.15, 126.58, 126.50, 125.07, 123.33, 119.79, 116.18, 114.93, 111.54, 55.60, 49.52, 37.11, 31.96, 31.79, 30.08, 29.80, 29.67, 29.39, 26.79, 22.74, 14.20. High-resolution mass spectroscopy (HRMS) (MALDI) *m/z*: calcd for C₈₈H₁₀₆N₄O₆S₂: 1378.7554; found: 1378.7519. Elemental Analysis (EA) (%) calcd for C₈₈H₁₀₆N₄O₆S₂: C, 76.59; H, 7.74; N, 4.06; found: C, 76.83; H, 7.61; N, 3.82.

2.2.2. Synthesis of L2-T

TPTI-Br (0.100 g, 0.107 mmol), compound **5a** (0.236 g, 0.349 mmol) and Pd(PPh₃)₄ (0.015 g, 0.013 mmol) in dry toluene (25 mL) was degassed with nitrogen for 30 min and then reacted at reflux for 24 h. After cooling to room temperature, the solution was extracted with CH₂Cl₂ and dried over anhydrous MgSO₄. The organic phase was concentrated by a rotary evaporator to get a brown solid. Then, the crude product was purified by column chromatography with petroleum ether/CH₂Cl₂ (1/1, v/v) as eluent to obtain L2-T (0.135 g, 82.3% yield) as a red solid. ¹H NMR (CDCl₃, 400 MHz, ppm) 8.67 (s, 2H), 7.40 (d, *J* = 8.5 Hz, 4H), 7.21 (m, 2H), 7.08 (m, 10H), 6.99 (s, 2H), 6.92 (d, *J* = 8.5 Hz, 4H), 6.85 (m, 8H), 4.19 (s, 4H), 3.82 (s, 12H), 2.01 (s, 2H), 1.51–1.07 (m, 48H), 0.92–0.72 (m, 12H). ¹³C NMR (CDCl₃, 101 MHz, ppm) 161.24, 156.21, 148.64, 144.93, 140.49, 139.41, 137.57, 134.28, 129.20, 126.91, 126.46, 126.33, 125.67, 125.52, 123.26, 122.35, 120.17, 116.10, 114.85, 112.61, 55.58, 49.30, 37.18, 32.01, 31.85, 31.79, 30.15, 29.85, 29.77, 29.45, 26.86, 22.77, 14.23, 14.20. HRMS (MALDI) *m/z*: calcd for C₉₆H₁₁₀N₄O₆S₄, 1542.7308; found: 1542.7374. EA (%) calcd for C₉₆H₁₁₀N₄O₆S₄: C, 74.67; H, 7.18; N, 3.63; found: C, 74.92; H, 7.14; N, 3.40.

2.3. Device fabrication

The indium tin oxide (ITO) glass substrates were cleaned by using detergent, distilled water, acetone, and isopropanol in sequence. Before the deposition of electron transport layers, the substrates were cleaned by ultraviolet ozone for 15 min. Then the SnO₂ nanoparticles (5%, diluted by water) were spin-coated on the substrates at 3000 r.p.m. for 20 s, and then annealed in ambient air at 120 °C for 10 min and 150 °C for 20 min. After cooling down to room temperature, the substrates were subjected to ultraviolet ozone treatment for 5 min and then transferred into a glove box. For the CsPbI₂Br perovskite film deposition, the perovskite solution was prepared by dissolving 276.6 mg of PbI₂, 220.2 mg of PbBr₂, and 311.8 mg of CsI in 1 mL of DMSO. Then, the solution was spin-coated onto the SnO₂ layer at 500 r.p.m. for 5 s and 3000 r.p.m. for 30 s, followed by thermal annealing via a two-step process at 42 °C for 30 s and 160 °C for 10 min, respectively. The HTMs (L2, L2-T, and Spiro-OMeTAD with a concentration of 20, 15, and 20 mg mL⁻¹, respectively.) were dissolved in chlorobenzene (CB) without additives. The hole-transporting layer was deposited on top of the perovskite layer at 3000 r.p.m. for 30 s. The resulting L2 and L2-T films were thermally annealed at 80 °C for 10 min to improve the device performance. Finally, 10 nm MoO₃ and 100 nm Ag cathode were deposited on the HTM layer.

2.4. Characterization of materials and devices

¹H NMR and ¹³C NMR spectra were measured on a Bruker AVANCE-400 spectrometer in CDCl₃ solutions with tetramethylsilane (TMS) as reference. HRMS measurements were carried out using Thermo Scientific Q Exactive HF Orbitrap-FTMS. Elemental analysis (EA) was performed by Elementar vario MACRO cube. Thermogravimetric analysis (TGA) was measured on Mettler TGA/SDTA851 at a heating rate of 20 °C min⁻¹. Differential scanning calorimetry (DSC) curves were recorded on Mettler DSC 822 at a heating rate of 10 °C min⁻¹. Ultraviolet–visible (UV–vis) spectra were collected on a Lambda 365 UV–vis spectrophotometer. Steady-state photoluminescence (PL) was measured by a fluorescence spectrometer (Edinburgh Instruments, FLS980). Ultraviolet

photoelectron spectra (UPS) for the thin films were carried out by using X-ray Photoelectron Spectroscopy (Thermo Fisher, ESCALAB 250Xi). Atomic Force Microscopy (AFM) measurements were conducted by using Bruker Dimension ICON in the tapping mode. The *J-V* characteristics of the devices were obtained using a Keithley 2400 Source Meter under simulated AM 1.5G illumination (100 mW cm^{-2}) with an Oriol Sol 3A simulator (Newport). The light intensity had been accurately calibrated with a National Renewable Energy Laboratory (NREL)-certified silicon reference cell. The external quantum efficiency (EQE) was measured with an EQE measurement system (Newport). The details of cyclic voltammetry (CV) and hole mobility measurements were provided in the Supporting Information.

3. Results and discussion

3.1. Synthesis

The synthetic routes of L2 and L2-T are shown in Scheme 1, and the details are afforded in the experimental section. Compounds **3a**, **5a** and the brominated monomer TPTI-Br were prepared according to the reported procedures [29,37,38]. Using $\text{Pd}(\text{PPh}_3)_4$ as catalyst, L2 was then synthesized in 81.6% yield through the Suzuki coupling reaction between TPTI-Br and compound **3a**. With the same palladium catalyst, the Stille coupling reaction between TPTI-Br and compound **5a** produced L2-T in 82.3% yield. The chemical structures of L2 and L2-T were characterized by ^1H NMR, ^{13}C NMR, HRMS, and EA, respectively. Both HTMs exhibit good solubility in common organic solvents such as dichloromethane, chlorobenzene, and toluene, implying their excellent solution processability.

3.2. Thermal stability

To investigate the thermal properties of L2 and L2-T, TGA and DSC measurements were conducted. From the TGA curves (Fig. S1), the decomposition temperatures (T_{d5}), defined as 5% mass loss, were estimated to be 420.5 and 446.6 °C for L2 and L2-T, respectively, suggesting their excellent thermal stability, which is essential for the operational stability of PVSCs in high temperature. As displayed in Fig. S2, both L2

and L2-T exhibit distinctly melting peaks and crystallization peaks, demonstrating high crystallinities for both of them in solid-state.

3.3. Photophysical and electrochemical properties

The optical absorption of L2 and L2-T were measured in dilute chloroform solution ($1.0 \times 10^{-5} \text{ M}$) and thin-film states, and the corresponding data are listed in Table 1. In solution, as shown in Fig. 1a, they both exhibit strong absorption bands in the visible region (400–550 nm), which mainly originates from the ICT transitions between donor unit and acceptor unit. The absorption peak (λ_{max}) of L2 is located at 450 nm. Nevertheless, L2-T shows a bathochromically shifted absorption with a λ_{max} of 480 nm, which could be attributed to the enhanced electron-donating effect induced by the thiophene spacers. The result can be further confirmed by the electrostatic surface potential (ESP) analysis, which was calculated by density functional theory (DFT) at B3LYP/6-311G** level. As shown in Fig. 1c and d, L2-T exhibits an extended negative electrostatic potential region in comparison with L2, suggesting an increased ICT in L2-T. In thin-film state, L2 and L2-T exhibit red-shifted absorption bands with distinct shoulder absorption peaks, indicating strong intermolecular interaction in films, which is in favor of efficient charge transfer. Meanwhile, the optical band gaps (E_{gapS}) of L2 and L2-T were calculated to be 2.25 and 2.10 eV, respectively, according to the onsets of absorption wavelength (λ_{onset}) in films. To further understand their Stokes shifts, PL spectra of L2 and L2-T were measured. As presented in Fig. S3, both of them reveal larger Stokes

Table 1
Photophysical and charge transport properties of L2 and L2-T.

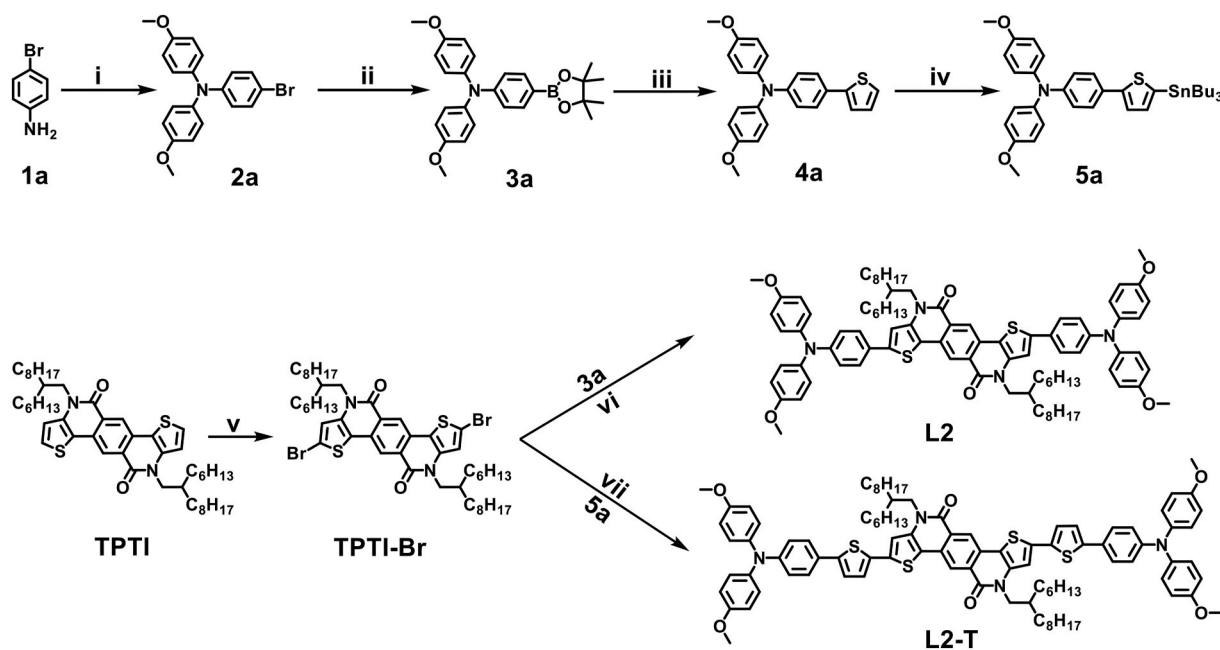
HTM	λ_{abs} (nm) ^a	E_{gap} (eV) ^b	E_{HOMO} (eV) ^c	E_{LUMO} (eV) ^d	μ ($\text{cm}^2 \text{V}^{-1} \text{s}^{-1}$)
L2	450	2.25	-4.95	-2.70	1.51×10^{-4}
L2-T	480	2.10	-4.77	-2.67	1.05×10^{-4}

^a Absorption spectra were measured in dilute chloroform solution.

^b Optical band gaps were calculated by the equation: $E_{\text{gap}} = 1240/\lambda_{\text{onset}}$ (eV).

^c E_{HOMO} in film was estimated by using the UPS measurement.

^d E_{LUMO} in film was calculated according to the equation of $E_{\text{HOMO}} = E_{\text{HOMO}} + E_{\text{gap}}$.



Scheme 1. Synthetic routes for L2 and L2-T: (i) 4-iodoanisole, CuI, KOH, 1,10-phenanthroline, toluene, reflux. (ii) bis(pinacolato)diboron, KOAc, $\text{Pd}(\text{dppf})\text{Cl}_2$, DMF, 80 °C. (iii) 2-bromothiophene, $\text{Pd}(\text{PPh}_3)_4$, K_2CO_3 , H_2O , toluene, 100 °C. (iv) *n*-BuLi, SnBu_3Cl , THF, -78 °C. (v) Br_2 , CHCl_3 , RT. (vi) $\text{Pd}(\text{PPh}_3)_4$, K_2CO_3 , toluene, H_2O , 100 °C. (vii) $\text{Pd}(\text{PPh}_3)_4$, toluene, reflux.

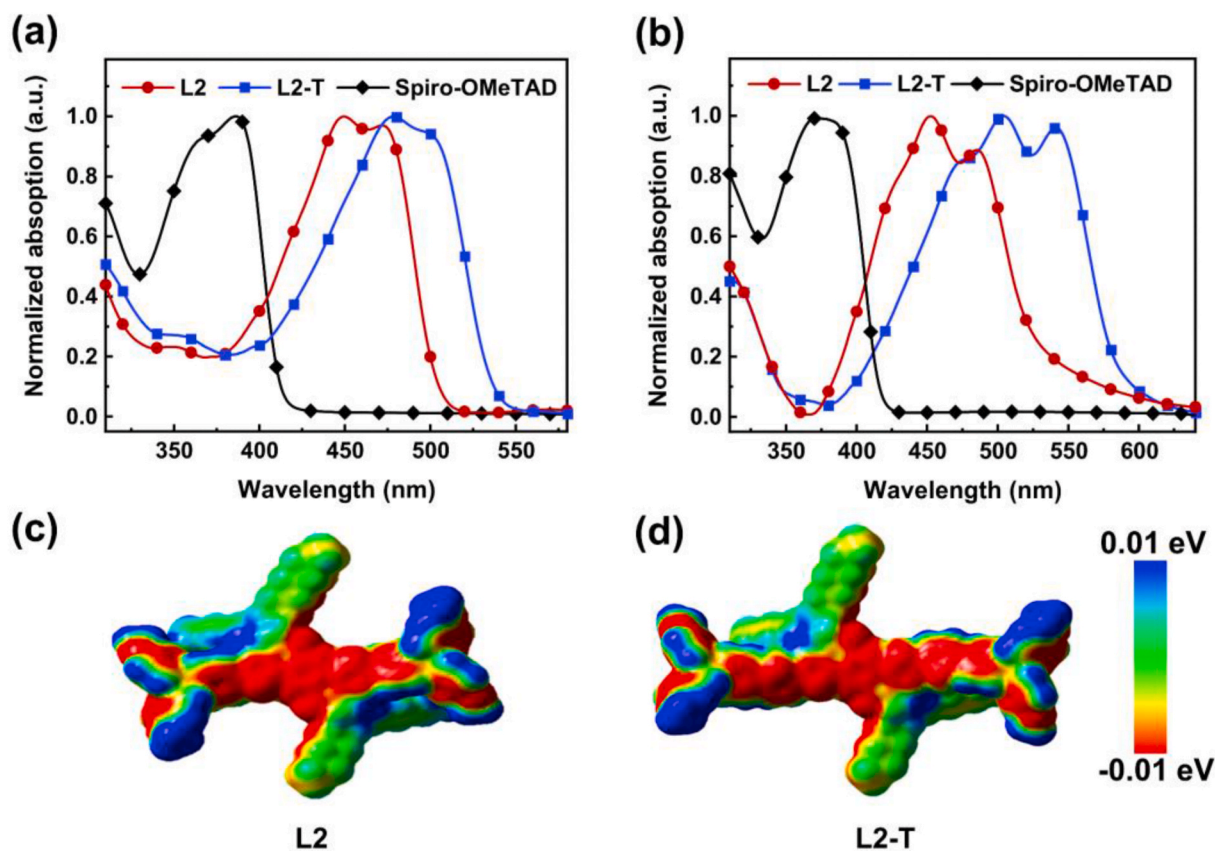


Fig. 1. The UV-vis absorption spectra of HTMs (a) in dilute chloroform solution and (b) in film. The electrostatic potential (ESP) of L2 (c) and L2-T (d).

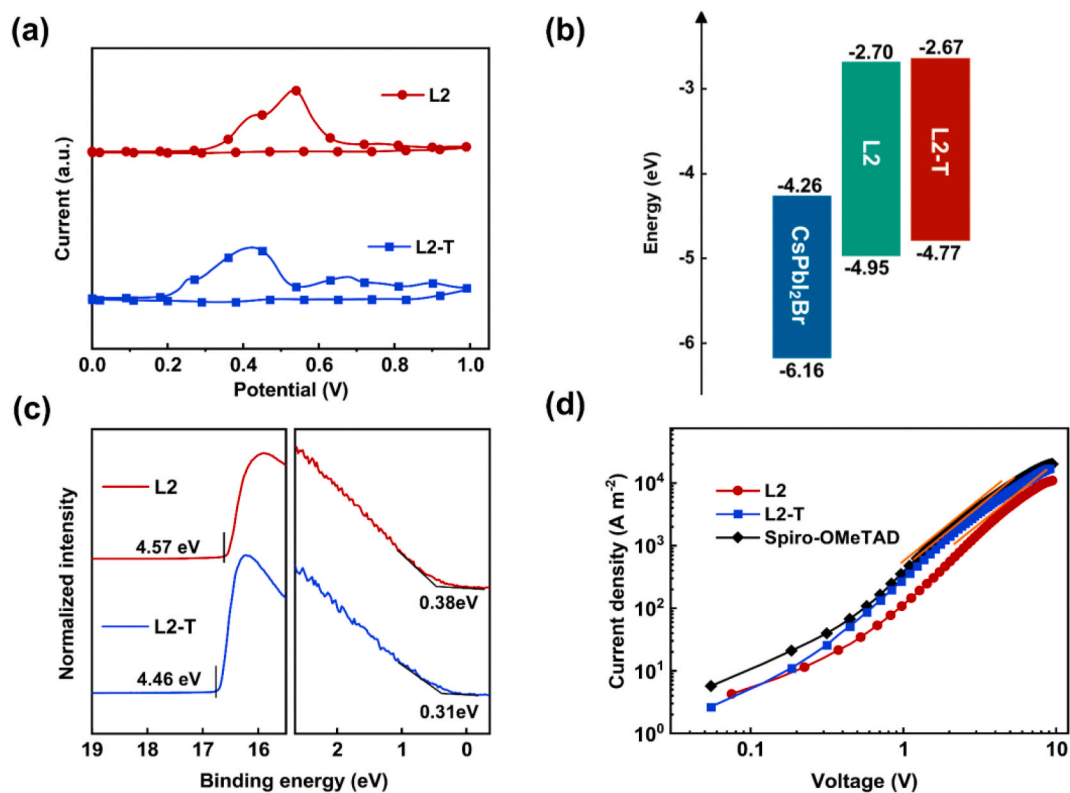


Fig. 2. (a) CV voltammograms of L2 and L2-T. (b) Energy level diagram of CsPbI₂Br, L2, and L2-T. (c) UPS spectra of L2 and L2-T films. (d) The J-V curves of hole-only devices based on L2, L2-T, and Spiro-OMeTAD, respectively.

shifts of around 120 nm compared with that of Spiro-OMeTAD (39 nm) [39], suggesting that they have significant structural deformation between ground state and excited state and a good molecular flexibility of the excited state, which is favorable for a better pore-filling of the HTMs with an improved hole extraction capability [40–42].

To further evaluate the electrochemical properties of L2 and L2-T, CV measurement was performed, and the CV curves are shown in Fig. 2a. The highest occupied molecular orbital (HOMO) energy levels were calculated according to the formula of $E_{\text{HOMO}} = -(\phi_{\text{ox}} + 4.82)$ (eV) with Fc/Fc^+ as an internal standard, where ϕ_{ox} is the onset oxidation potential. For L2, the HOMO energy level was estimated to be -5.12 eV. Whereas, L2-T displays an up-shifted HOMO energy level of -5.02 eV due to the electron-donating thiophene spacers. Moreover, the UPS measurement was further employed to determine the energy levels in films. The cut-off regions and the onset regions for L2 and L2-T are shown in Fig. 2c. The energetic gaps between Fermi levels (E_{F}) and HOMO energy levels were estimated to be 0.38 and 0.31 eV for L2 and L2-T, respectively. Meanwhile, the corresponding work functions were evaluated to be 4.57 and 4.46 eV. Thus, the HOMO energy levels were determined to be -4.95 and -4.77 eV for L2 and L2-T in the film state, respectively, which are in agreement with the results from the CV measurements. In the two HTMs, L2 exhibits a deeper-lying HOMO energy level, which could contribute to enhanced hole transfer and reduced energy loss. On the other hand, the lowest unoccupied molecular orbital (LUMO) energy levels of L2 and L2-T in film-states were calculated to be -2.70 and -2.67 eV, respectively, according to the equation of $E_{\text{LUMO}} = E_{\text{HOMO}} + E_{\text{gap}}$. Compared with the conduction band of CsPbI_2Br perovskite (-4.26 eV) [43], the LUMO energy levels of L2 and L2-T are high enough to block the electrons transfer from the conduction band of perovskite to the back-metal electrode.

3.4. Film morphologies and charge transport properties

The tapping mode AFM was conducted to probe the morphologies of the small-molecule films when coated on the surface of perovskite. As shown in Fig. 3, the root-mean-square (RMS) roughnesses of L2, L2-T and Spiro-OMeTAD films were determined to be 2.5, 3.9, and 4.2 nm, respectively, significantly lower than the value of 21.2 nm for pristine

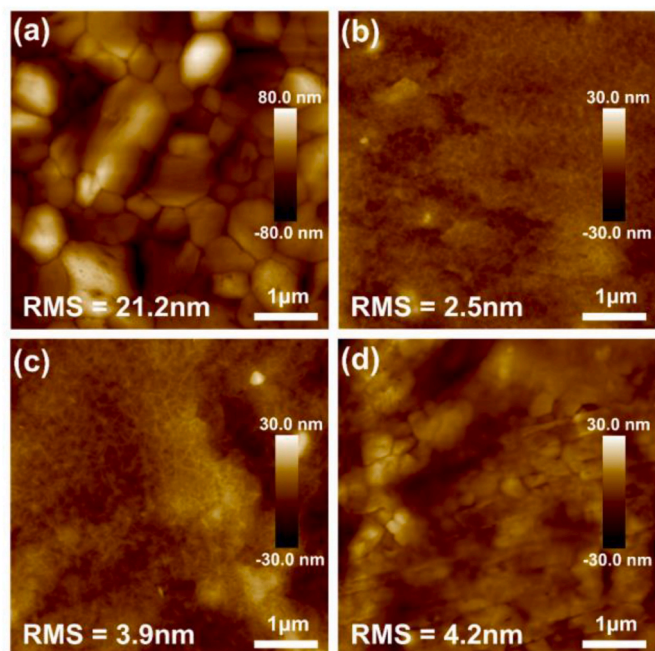


Fig. 3. AFM height images of (a) the pristine perovskite and the perovskites coated with (b) L2, (c) L2-T, and (d) Spiro-OMeTAD.

perovskite film. Particularly, the L2 film exhibits a smooth and uniform morphology with the smallest RMS value, which is expected to form better ohmic contact between perovskite film and electrode thereby reducing undesirable current leakage in the resulting PVSCs.

To study the charge transport properties of L2 and L2-T, the hole mobilities (μ) were measured with the architecture of ITO/poly(3,4-ethylenedioxythiophene) polystyrenesulfonate (PEDOT:PSS)/HTM/ MoO_3/Ag through space-charge-limited current (SCLC) method, and the J - V curves are shown in Fig. 2d. The μ of dopant-free L2 film was evaluated to be $1.51 \times 10^{-4} \text{ cm}^2 \text{ V}^{-1} \text{ s}^{-1}$, slightly larger than that of L2-T film ($1.05 \times 10^{-4} \text{ cm}^2 \text{ V}^{-1} \text{ s}^{-1}$), which can be partly ascribed to the smooth and uniform morphology of the L2 film. Under the same device fabrication conditions, the Spiro-OMeTAD film affords significantly reduced μ of $1.40 \times 10^{-5} \text{ cm}^2 \text{ V}^{-1} \text{ s}^{-1}$. The enhanced charge transport property for L2 and L2-T is beneficial for efficient charge transfer and low charge recombination.

3.5. Photovoltaic performance

To investigate the photovoltaic performances of L2 and L2-T, typical n-i-p devices were prepared with the architecture of ITO/ $\text{SnO}_2/\text{CsPbI}_2\text{Br}/\text{HTM}/\text{MoO}_3/\text{Ag}$ (Fig. 4a). The J - V curves of PVSCs based on three HTMs are shown in Fig. 4b, and the corresponding parameters are tabulated in Table 2. The best-performing device based on L2 exhibits an impressive PCE of 12.41% with a V_{OC} of 1.21 V, a J_{SC} of 13.73 mA cm^{-2} , and a FF of 75.02%. By contrast, the L2-T-based counterpart shows a relatively low PCE of 11.07% with a V_{OC} of 1.16 V, a J_{SC} of 13.56 mA cm^{-2} , and a FF of 70.63%. It can be found that L2-based device presents increased V_{OC} and FF values than those of the device using L2-T as HTM. The reason for the higher V_{OC} in L2-based device is probably related with the deeper-lying HOMO level of L2. On the other hand, L2-based device delivers a shunt resistance (R_{sh}) of $8.19 \text{ k}\Omega \text{ cm}^2$ and a series resistance (R_s) of $7.82 \Omega \text{ cm}^2$ (Table 2). Whereas, the device based on L2-T shows an inferior ohmic contact with a reduced R_{sh} of $3.63 \text{ k}\Omega \text{ cm}^2$ and an increased R_s of $9.22 \Omega \text{ cm}^2$, which is partly responsible for its decreased FF. The lower R_{sh} and higher R_s of L2-T-based device could be attributed to the rougher morphology and lower hole mobility of L2-T, which would increase charge recombination and leakage current in the surface and restrain the hole transfer between perovskite layer and HTM [44–46]. For the comparison purpose, the devices with dopant-free Spiro-OMeTAD were fabricated under the same conditions, and the corresponding PCE decreased to 9.95% with a V_{OC} of 1.16 V, a J_{SC} of 13.77 mA cm^{-2} and a FF of 62.51%. The EQE spectra for the devices were measured to verify the accuracy of the J_{SC} values obtained from the J - V curves. As shown in Fig. 4c, both L2- and L2-T-based devices show strong photon-response in the wavelength range from 350 nm to 650 nm. The integrated J_{SC} values for L2-, L2-T-, and Spiro-OMeTAD-based devices were estimated to be 13.62, 13.37, and 13.71 mA cm^{-2} , respectively, which agree with the results from the J - V curves within 2% mismatches. Additionally, the stabilized power output efficiencies of the devices based on L2, L2-T, and Spiro-OMeTAD were recorded. As shown in Fig. S5, under the maximum power-point conditions and 400 s continuous illumination, the stabilized PCEs of L2-, L2-T-, and Spiro-OMeTAD-based devices were 11.82%, 10.53%, and 9.34%, respectively, which agree with the results from the J - V scan. It can be found that both L2- and L2-T-based devices could maintain over 95% of their initial values after 400 s of operation. Whereas, the device based on Spiro-OMeTAD exhibited relatively poor stability, whose PCE decreased by more than 5%, indicating the better operational stability of the L2- and L2-T-based PVSCs.

3.6. Hydrophobic properties and long-term stability of devices

The contact angle tests were performed to analyze the surface wettability of HTMs. As shown in Fig. S4, L2 and L2-T reveal strong hydrophobic properties with contact angles of 92.2° and 92.5° ,

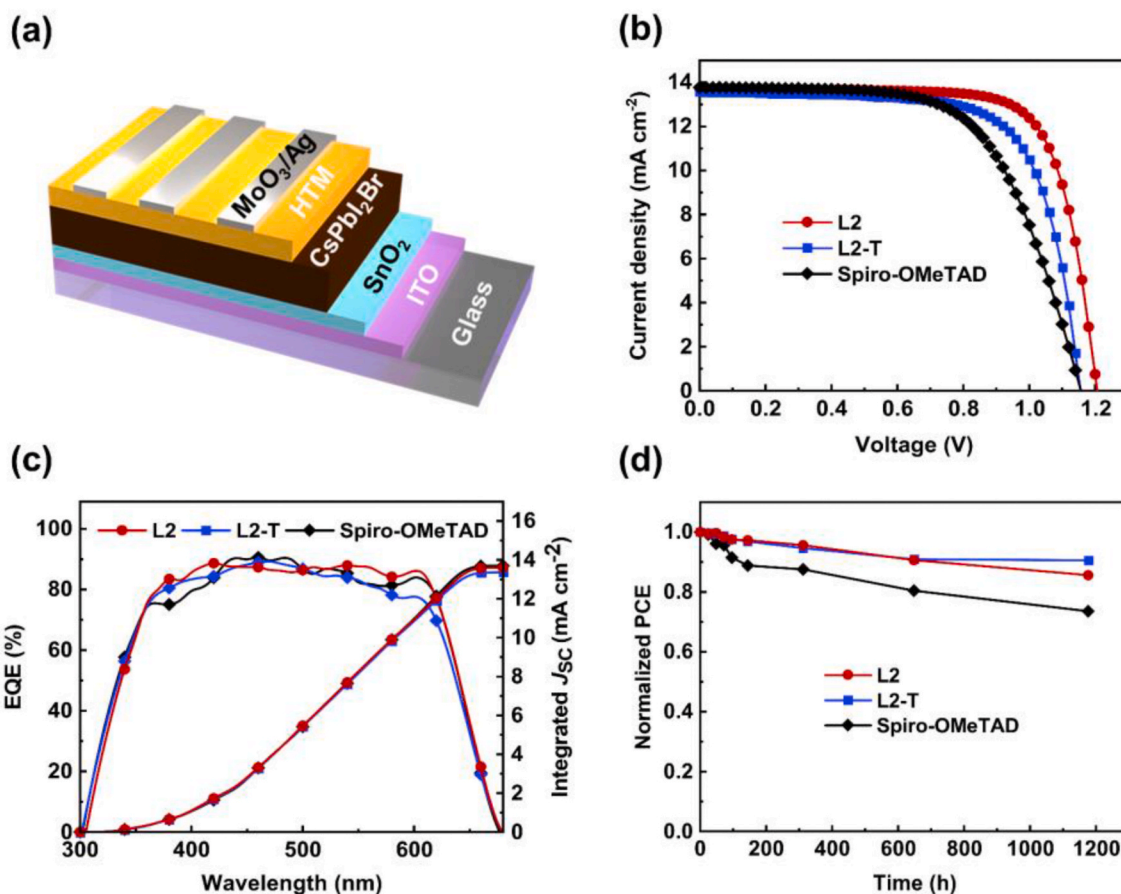


Fig. 4. (a) Schematic diagram of the device structure with n-i-p configuration. (b) J - V curves of the optimized devices based on L2, L2-T, and Spiro-OMeTAD. (c) Corresponding EQE spectra, and (d) long-term stability of the encapsulated devices in air.

Table 2

Photovoltaic parameters of the devices based on L2, L2-T, and Spiro-OMeTAD.

HTM	V_{oc} (V) ^a	J_{sc} (mA cm ⁻²)	FF (%)	PCE (%)	R_s (Ω cm ²)	R_{sh} (k Ω cm ²)
L2	1.21 (1.19 ± 0.01)	13.73 (13.39 ± 0.37)	75.02 (73.39 ± 2.35)	12.41 (11.73 ± 0.42)	7.82	8.19
L2-T	1.16 (1.14 ± 0.01)	13.56 (13.34 ± 0.50)	70.63 (67.68 ± 2.42)	11.07 (10.32 ± 0.47)	9.22	3.63
Spiro-OMeTAD	1.16 (1.14 ± 0.02)	13.77 (13.38 ± 0.69)	62.51 (59.46 ± 3.13)	9.95 (9.05 ± 0.47)	17.54	7.56

^a In the parentheses are average values based on more than 20 devices.

respectively, which is beneficial for improving the stability of the corresponding devices. However, Spiro-OMeTAD is of relatively weak hydrophobic nature with a reduced contact angle of 76.5°. The long-term stability of PVSCs with encapsulation was measured in air at room temperature. As shown in Fig. 4d, the device based on L2 maintained over 85% of its initial PCE after 1000 h. Meanwhile, L2-T-based device displayed relatively better stability than L2, retaining over 90% of its original PCE at the same storage conditions. In contrast, the device based on dopant-free Spiro-OMeTAD revealed relatively inferior stability by maintaining 73% of its original PCE under the same conditions.

4. Conclusion

In summary, two novel D-A-D type dopant-free HTMs (L2 and L2-T) were designed and synthesized using ladder-type TPTI as the acceptor unit and TPA groups as donor units. The planar molecular structure can significantly strength the intermolecular π - π stacking, leading to an excellent charge transport property. Finally, L2 and L2-T showed higher

hole mobilities than Spiro-OMeTAD. The CsPbI₂Br PVSC based on L2 showed the highest PCE of 12.41% due to its well-matched energy levels, smooth film morphology, and increased hole mobility. Whereas, the device based on dopant-free Spiro-OMeTAD displayed a relatively low PCE of 9.95%. Moreover, both dopant-free L2- and L2-T-based devices could maintain over 85% of their initial PCEs after 1000 h storage suggesting their excellent shelf-storage stability. These results indicate that the ladder-type TPTI is a promising building block to construct D-A-D type HTMs for efficient and stable CsPbI₂Br PVSCs.

CRediT authorship contribution statement

Hao Liu: synthesized the hole-transporting materials, fabricated and tested the solar cell devices, wrote the manuscript. **Qisheng Tu:** fabricated and tested the solar cell devices, wrote the manuscript. **Di Wang:** fabricated and tested the solar cell devices, All authors discussed the results and commented on the final manuscript. **Qingdong Zheng:** designed the experiments, wrote the manuscript, directed this project.

Declaration of competing interest

The authors declare that they have no known competing financial interests or personal relationships that could have appeared to influence the work reported in this paper.

Acknowledgements

We thank financial support from the National Natural Science Foundation of China (No. U1605241), the Natural Science Foundation of Fujian Province for Distinguished Young Scholars (No. 2019J06023), the Key Research Program of Frontier Sciences, CAS (No. QYZDB-SSW-SLH032).

Appendix A. Supplementary data

Supplementary data to this article can be found online at <https://doi.org/10.1016/j.dyepig.2021.109368>.

References

- Kojima A, Teshima K, Shirai Y, Miyasaka T. Organometal halide perovskites as visible-light sensitizers for photovoltaic cells. *J Am Chem Soc* 2009;131(17):6050–1.
- NREL Best research-cell efficiencies chart. 2020. Available from: <https://www.nrel.gov/pv/assets/pdfs/best-research-cell-efficiencies.20200218.pdf>.
- Ouedraogo NAN, Chen Y, Xiao YY, Meng Q, Han CB, Yan H, et al. Stability of all-inorganic perovskite solar cells. *Nano Energy* 2020;67:104249.
- Berhe TA, Su W, Chen C, Pan C, Cheng J, Chen HM, Tsai MC, Chen LY, Dubale AA, Hwang BJ. Organometal halide perovskite solar cells: degradation and stability. *Energy Environ Sci* 2016;9(2):323–56.
- Zhang JR, Hodes G, Jin ZW, Liu SZ. All-Inorganic CsPbX₃ perovskite solar cells: progress and prospects. *Angew Chem Int Ed* 2019;58(44):15596–618.
- Xiao Q, Tian JJ, Xue QF, Wang J, Xiong BJ, Han MM, Li Z, Zhu ZL, Yip HL, Li ZA. Dopant-free squaraine-based polymeric hole-transporting materials with comprehensive passivation effects for efficient all-inorganic perovskite solar cells. *Angew Chem Int Ed* 2019;58(49):17724–30.
- Yoon SM, Min H, Kim JB, Kim G, Lee KS, Seok SI. Surface engineering of ambient-air-processed cesium lead triiodide layers for efficient solar cells. *Joule* 2020;5(1):183–96.
- Ma JJ, Li YH, Li J, Qin MC, Wu X, Lv ZY, et al. Constructing highly efficient all-inorganic perovskite solar cells with efficiency exceeding 17% by using dopant-free polymeric electron-donor materials. *Nano Energy* 2020;75:104933.
- Chen SC, Wang D, Zheng QD. Surface passivation of all-inorganic CsPbI₂Br with a fluorinated organic ammonium salt for perovskite solar cells with efficiencies over 16%. *Sol RRL* 2020;4(10):2000321.
- Tian JJ, Xue QF, Tang XF, Chen YX, Li N, Hu ZC, Shi TT, Wang X, Huang F, Brabec CJ, Yip HL, Cao Y. Dual interfacial design for efficient CsPbI₂Br perovskite solar cells with improved photostability. *Adv Mater* 2019;31(23):1901152.
- Jeong MY, Choi IW, Go EM, Cho YJ, Kim MJ, Lee BK, Jeong SH, Jo YH, Choi HW, Lee JY, Bae JH, Kwak SK, Kim DS, Yang CD. Stable perovskite solar cells with efficiency exceeding 24.8% and 0.3 V voltage loss. *Science* 2020;369(6511):1615–20.
- Christians JA, Schulz P, Tinkham JS, Schloemer TH, Harvey SP, Tremolet de Villers BJ, Sellinger A, Berry JJ, Luther JM. Tailored interfaces of unencapsulated perovskite solar cells for >1,000 hour operational stability. *Nat Energy* 2018;3(1):68–74.
- Hou Y, Du XY, Scheiner S, McMeekin DP, Wang ZP, Li N, Killian MS, Chen HW, Richter M, Levchuk I, Schrenker N, Spiecker E, Stubhan T, Luechinger NA, Hirsch A, Schmuki P, Steinruck HP, Fink RH, Halik M, Snaith HJ, Brabec CJ. A generic interface to reduce the efficiency-stability-cost gap of perovskite solar cells. *Science* 2017;358(6367):1192–7.
- Pham HD, Yang TCJ, Jain SM, Wilson GJ, Sonar P. Development of dopant-free organic hole transporting materials for perovskite solar cells. *Adv Energy Mater* 2020;10(13):1903326.
- Saragi TPI, Spehr T, Siebert A, Fuhrmann Lieker T, Salbeck J. Spiro compounds for organic optoelectronics. *Chem Rev* 2007;107(4):1011–65.
- Urieta Mora J, Garcia Benito I, Molina Ontoria A, Martin N. Hole transporting materials for perovskite solar cells: a chemical approach. *Chem Soc Rev* 2018;47(23):8541–71.
- Li ZA, Zhu ZL, Chueh CC, Jo SB, Luo JD, Jang SH, Jen AK. Rational design of dipolar chromophore as an efficient dopant-free hole-transporting material for perovskite solar cells. *J Am Chem Soc* 2016;138(36):11833–9.
- Wang Y, Liao QG, Chen JH, Huang W, Zhuang XM, Tang YM, Li BL, Yao XY, Feng XY, Zhang XH, Su MY, He ZB, Marks TJ, Facchetti A, Guo XG. Teaching an old anchoring group new tricks: enabling low-cost, eco-friendly hole-transporting materials for efficient and stable perovskite solar cells. *J Am Chem Soc* 2020;142(39):16632–43.
- Yu XY, Li Z, Sun XL, Zhong C, Zhu ZL, Li ZA, et al. Dopant-free dicyanofluoranthene-based hole transporting material with low cost enables efficient flexible perovskite solar cells. *Nano Energy* 2021;82:105701.
- Wang Y, Chen W, Wang L, Tu B, Chen T, Liu B, Yang K, Koh CW, Zhang XH, Sun H, Chen GC, Feng XY, Woo HY, Djuricic AB, He ZB, Guo XG. Dopant-free small-molecule hole-transporting material for inverted perovskite solar cells with efficiency exceeding 21%. *Adv Mater* 2019;31(35):1902781.
- Guo HX, Zhang H, Shen C, Zhang DW, Liu SJ, Wu YZ, Zhu WH. A coplanar π -extended quinoxaline based hole-transporting material enabling over 21% efficiency for dopant-free perovskite solar cells. *Angew Chem Int Ed* 2020;60(5):2674–9.
- Tian Y, Tao L, Chen C, Lu HF, Li HP, Yang XC, Cheng M. Facile synthesized fluorine substituted benzothiadiazole based dopant-free hole transport material for high efficiency perovskite solar cell. *Dyes Pigments* 2021;184:108786.
- Zhou X, Kong FT, Sun Y, Huang Y, Zhang XX, Ghadari R. Dopant-free benzothiadiazole bridged hole transport materials for highly stable and efficient perovskite solar cells. *Dyes Pigments* 2020;173:107954.
- Ye XX, Zhao XJ, Li QY, Ma YF, Song WW, Quan YY, Wang ZC, Wang MK, Huang ZS. Effect of the acceptor and alkyl length in benzotriazole-based donor-acceptor-donor type hole transport materials on the photovoltaic performance of PSCs. *Dyes Pigments* 2019;164:407–16.
- Liu F, Wu F, Tu ZX, Liao QY, Gong YB, Zhu LN, Li QQ, Li Z. Hole transport materials based on 6,12-dihydroindeno[1,2-b]fluorine with different periphery groups: a new strategy for dopant-free perovskite solar cells. *Adv Funct Mater* 2019;29(24):1901296.
- Wu JS, Cheng SW, Cheng YJ, Hsu CS. Donor-acceptor conjugated polymers based on multifused ladder-type arenes for organic solar cells. *Chem Soc Rev* 2015;44(5):1113–54.
- Ma YL, Zhang MQ, Yan Y, Xin JM, Wang T, Ma W, Tang CQ, Zheng QD. Ladder-type dithienonaphthalene-based small-molecule acceptors for efficient nonfullerene organic solar cells. *Chem Mater* 2017;29(18):7942–52.
- Tu QS, Tang CQ, Zheng QD. Ladder-type dithienocyclopentadibenzothiophene-cored wide-bandgap polymers for efficient non-fullerene solar cells with large open-circuit voltages. *J Mater Chem A* 2019;7(7):3307–16.
- Cao JM, Liao QG, Du XY, Chen JH, Xiao Z, Zuo QQ, Ding LM. A pentacyclic aromatic lactam building block for efficient polymer solar cells. *Energy Environ Sci* 2013;6(11):3224–8.
- Chen L, Yin P, Zeng X, Weng C, Chen Y, Cui C, et al. Low-bandgap D-A1-D-A2 type copolymers based on TPPI unit for efficient fullerene and nonfullerene polymer solar cells. *Polymer* 2019;182:121850.
- Zhang F, Zhu K. Additive engineering for efficient and stable perovskite solar cells. *Adv Energy Mater* 2019;10(13):1902579.
- Noel NK, Abate A, Stranks SD, Parrott ES, Burlakov VM, Goriely A, Snaith HJ. Enhanced photoluminescence and solar cell performance via Lewis base passivation of organic-inorganic lead halide perovskites. *ACS Nano* 2014;8(10):9815–21.
- Peng J, Khan JI, Liu WZ, Ugur E, Duong T, Wu YL, Shen HP, Wang K, Dang H, Aydin E, Yang XB, Wan YM, Weber KJ, Catchpole KR, Laquai F, De Wolf S, White TP. A universal double-side passivation for high open-circuit voltage in perovskite solar cells: role of carbonyl groups in poly(methyl methacrylate). *Adv Energy Mater* 2018;8(30):1801208.
- Zhou J, Yin XX, Dong ZH, Ali A, Song ZN, Shrestha N, et al. Dithieno[3,2-b:2',3'-d]pyrrole cored p-type semiconductors enabling 20% efficiency dopant-free perovskite solar cells. *Angew Chem Int Ed* 2019;131(39):13855–9.
- Kim GW, Choi H, Kim MJ, Lee JW, Son SY, Park TH. Hole transport materials in conventional structural (n-i-p) perovskite solar cells: from past to the future. *Adv Energy Mater* 2020;10(8):1903403.
- Wang JY, Liu K, Ma LC, Zhan XW. Triarylamine: versatile platform for organic, dye-sensitized, and perovskite solar cells. *Chem Rev* 2016;116(23):14675–725.
- Wu YG, Wang ZH, Liang M, Cheng H, Li MY, Liu LY, Wang BY, Wu JH, Prasad Ghimire R, Wang XD, Sun Z, Xue S, Qiao QQ. Influence of nonfused cores on the photovoltaic performance of linear triphenylamine-based hole-transporting materials for perovskite solar cells. *ACS Appl Mater Interfaces* 2018;10(21):17883–95.
- Li TY, Su C, Akula SB, Sun WG, Chien HM, Li WR. New pyridinium ylide dyes for dye sensitized solar cell applications. *Org Lett* 2016;18(14):3386–9.
- Chen J, Xia JX, Gao WJ, Yu HJ, Zhong JX, Jia CY, et al. Tetraphenylbutadiene-based symmetric 3D hole-transporting materials for perovskite solar cells: a trial trade-off between charge mobility and film morphology. *ACS Appl Mater Interfaces* 2020;12(18):21088–99.
- Li HR, Fu KW, Hagfeldt A, Gratzel M, Mhaisalkar SG, Grimsdale AC. A simple 3,4-ethylenedioxythiophene based hole-transporting material for perovskite solar cells. *Angew Chem Int Ed* 2014;53(16):4085–8.
- Alberga D, Mangiatordi GF, Labat F, Ciofini I, Nicolotti O, Lattanzi G, Adamo C. Theoretical investigation of hole transporter materials for energy devices. *J Phys Chem C* 2015;119(42):23890–8.
- Pham HD, Do TT, Kim J, Charbonneau C, Manzhos S, Feron K, Tsoi WC, Durrant JR, Jain SM, Sonar P. Molecular engineering using an anthanthrone dye for low-cost hole transport materials: a strategy for dopant-free, high-efficiency, and stable perovskite solar cells. *Adv Energy Mater* 2018;8(16):1703007.
- Lu JJ, Chen SC, Zheng QD. Defect passivation of CsPbI₂Br perovskites through Zn (II) doping: toward efficient and stable solar cells. *Sci China Chem* 2019;62(8):1044–50.

- [44] Mabrouk S, Zhang MM, Wang ZH, Liang M, Bahrami B, Wu YG, et al. Dithieno[3,2-*b*:2',3'-*d*]pyrrole-based hole transport materials for perovskite solar cells with efficiencies over 18%. *J Mater Chem A* 2018;6(17):7950–8.
- [45] Singh R, Sandhu S, Lee JJ. Elucidating the effect of shunt losses on the performance of mesoporous perovskite solar cells. *Sol Energy* 2019;193:956–61.
- [46] Tvingstedt K, Gil-Escrig L, Momblona C, Rieder P, Kiermasch D, Sessolo M, Baumann A, Bolink HJ, Dyakonov V. Removing leakage and surface recombination in planar perovskite solar cells. *ACS Energy Lett* 2017;2(2):424–30.